JGR Solid Earth

RESEARCH ARTICLE
10.1029/2023JB026795

A Scaling for the Permeability of Loose Magma Mush Validated Using X-Ray Computed Tomography of Packed Confectionary in 3D and Estimation Methods From 2D Crystal Shapes

Eloïse Bretagne[1], Fabian B. Wadsworth[1], Jérémie Vasseur[2], and Katherine J. Dobson[3]

[1]Earth Sciences, Durham University, Durham, UK, [2]Earth and Environmental Sciences, Ludwig-Maximilians-Universität, Munich, Germany, [3]Department of Civil and Environmental Engineering, University of Strathclyde, Glasgow, UK

Key Points:

- Crystal shape exerts a first order control on magma mush permeability
- The specific surface area of magmatic crystals is the relevant metric to predict the permeability, across all crystal shapes
- Magma mush permeability can be calculated from crystal size measurements made on a 2D thin section, via a 2D-to-3D conversion

Correspondence to:

E. Bretagne,
eloise.bretagne@durham.ac.uk

Citation:

Bretagne, E., Wadsworth, F. B., Vasseur, J., & Dobson, K. J. (2023). A scaling for the permeability of loose magma mush validated using X-ray computed tomography of packed confectionary in 3D and estimation methods from 2D crystal shapes. *Journal of Geophysical Research: Solid Earth*, *128*, e2023JB026795. https://doi.org/10.1029/2023JB026795

Received 6 APR 2023
Accepted 19 SEP 2023

Author Contributions:

Conceptualization: Eloïse Bretagne, Fabian B. Wadsworth
Formal analysis: Eloïse Bretagne, Jérémie Vasseur
Methodology: Eloïse Bretagne
Supervision: Fabian B. Wadsworth, Jérémie Vasseur, Katherine J. Dobson
Visualization: Eloïse Bretagne
Writing – original draft: Eloïse Bretagne, Fabian B. Wadsworth, Jérémie Vasseur
Writing – review & editing: Eloïse Bretagne, Fabian B. Wadsworth, Jérémie Vasseur, Katherine J. Dobson

Abstract Melt percolation through partially molten "mushy" regions of the crust underpins models for magma migration, accumulation, and processes that prime systems for eruption. Knowledge of the hydraulic properties of magma mush, specifically permeability, is required for accurate predictions of melt migration rates and accumulation timescales. Previous studies, validated for cuboidal crystal analogs, show that crystal shape exerts a first-order control on the permeability, and is tested here for anisometric natural crystal shapes using X-ray CT 3D data sets of magma mush analogs made from packed confectionary particles arranged randomly. We use a lattice-Boltzmann fluid flow simulation tool to determine the permeability of the analogue melt phase network between the packed particles. We find excellent agreement with our data sets to within ~0.1 log units, when the specific surface area is measured. To extend this to more typical cases where the specific surface area is unknown, we use the shape and size of the objects determined in both 3D and 2D to estimate the specific surface area assuming a cuboid approximation. These approximate solutions give good results to within ~0.5 log units of the measured permeability and offer a method by which permeability could be estimated from a thin section of a cumulate or pluton sample. Our shape-sensitive approach is more accurate than existing models for permeability of magma mush, most approximating natural crystal shapes to spheres. We therefore propose that these could be implemented in dynamic magma mush models for melt movement in the crust to produce more accurate flux predictions.

Plain Language Summary Magma chambers in the Earth are "mushy," meaning that liquid magma is trapped in between solid crystals. In many cases, the liquid magma must escape before an eruption occurs. For the liquid magma to escape, it must move through the tight spaces between the solid crystals, which occurs at a speed dictated by the "permeability" of the crystal framework. Here, we use fudge and sugar crystals as a proxy for the solid crystals in these magma chambers, and we use simulations to observe how the fluid between the fudge and sugar moves. The key advance here is that we show how the complicated shape of fudge and sugar crystals changes the speed at which the fluid is able to move.

1. Introduction

The dynamics of magma movement through the Earth's crust remain poorly understood. The leading models contend that magmas accumulate in the upper crust through repeated intrusive emplacement as mush—a mixture of crystals and melt in varying proportions. Magma mush is defined as a semi-rigid framework of packed and variably intergrown or overgrown crystals with an interstitial melt phase (Cashman et al., 2017; Sparks et al., 2019). Upon emplacement in the crust, melts can migrate relative to and through the magma mush (Annen, 2009; Bachmann & Bergantz, 2004; Cashman et al., 2017; Jackson et al., 2018; Sparks et al., 2019). Therefore, for large portions of the system, the advection of melt from one place to another is hosted in a porous medium, the solid static framework of which is a complex 3D manifold of crystal phases. This means a key parameter that can limit the rates and fluxes of melt through the system is the permeability of the mush. All crust-scale models require permeability to compute fluxes (Bachmann & Bergantz, 2004; Jackson et al., 2018) and yet there is relatively little work constraining mush permeability and how it evolves (Bretagne et al., 2023; Cheadle et al., 2004; Hersum, 2009; Hersum et al., 2005).

While the exact physical processes are debated (cf. Holness, 2018; Liu & Lee, 2021), the extraction of melts from mushes primes some magmatic systems to erupt voluminous crystal-poor silicic magmas in very large eruptions (Bachmann & Bergantz, 2004; Hildreth & Wilson, 2007; Wilson et al., 2021). Therefore, while understanding mush permeability is important for predicting melt migration in general, it may also hold the key to understanding the timescales of melt extraction prior to Earth's largest eruptions.

"Magma mush" is a term that is used in different ways in published work but in most cases a "mush" refers to a magma with a crystallinity above a certain threshold value. Generally speaking, this threshold value is thought to represent the demarcation between (a) a suspension of crystals in a melt-dominated magma, and (b) a framework of crystals with interstitial melt; the latter being a "mush" (Dufek & Bachmann, 2010; Tramontano et al., 2017). Here, we follow Bretagne et al. (2023) in defining a "loose mush" in terms of a crystallinity range $\phi_\tau \leq \phi \leq \phi_j$, where ϕ is the crystal volume fraction in the magma, ϕ_τ is the lowest value of ϕ where crystal-crystal interactions become important and a yield stress manifests, and ϕ_j is the upper bound of the "loose mush" definition where crystals are jammed at what is sometimes called the maximum packing. Importantly, $\phi_j < 1$, meaning that there are other regions of the "mush" definition at $\phi > \phi_j$ where crystal intergrowths or overgrowths, or nucleation of phases in the interstices of packed crystal frameworks become important. Bretagne et al. (2023) showed that the values of ϕ_τ and ϕ_j depend on crystal shape, with important implications for the controls of mush mineralogy on the evolving properties of mush.

Typically, the permeability k of mushy magma is predicted using a general scaling such as $k = a^2\beta\phi_m^3$ (Jackson et al., 2018), where a is the crystal "size" (usually radius), ϕ_m is the melt fraction interstitial to the crystals (such that $\phi_m = 1 - \phi$ in a two-phase crystal-melt system), and β is a constant. This approach encompasses the widely used Kozeny-Carman formulation $k = \phi_m^3 a^2/\left(150(1-\phi_m)^2\right)$, for which $\beta = 1/\left(150(1-\phi_m)^2\right)$ (e.g., Bachmann & Bergantz, 2004). In these models, complex crystal habits and multi-component mushes are reduced to a single size parameter a, despite evidence that the shape of the objects defining the solid framework in a porous medium has a first-order effect on the possible packing geometries (e.g., Liu et al., 2017) and the resulting permeability at those packings (Bretagne et al., 2023). Here, we move beyond idealized shapes and test more sophisticated permeability models against packs of realistic particles explicitly. Our aim is to constrain the efficacy of magma mush permeability models.

2. A Permeability Model for Loose Mush

The simplest and most widely used model for the permeability k of packed particles is the Kozeny-Carman model (Ergun, 1952). While this model is given in a variety of forms, sometimes including additional parameters such as a pore network tortuosity, and the specific lengths of pores or particles, the more general form is

$$k = \frac{\phi_m^3}{Cs^2} \tag{1}$$

where ϕ_m is the volume fraction of the non-particle phase, C is a constant, and s is the specific surface area of the pore space (Torquato, 2013; Röding et al., 2020; Vasseur & Wadsworth, 2017; Wadsworth et al., 2017; Vasseur et al., 2021, 2022). In the case of magma mush, we can think of ϕ_m as being the melt volume fraction, and then $\phi = 1 - \phi_m$ representing the crystal volume fraction (assuming a two-phase system). In general, across a very wide range of porous media, $C \approx 5$ appears to result in a good match between Equation 1 and empirical data when the medium is statistically representative and isotropic (Torquato, 2013; Vasseur et al., 2021). Since C appears independent of the medium, and ϕ can be readily determined using image analysis tools or laboratory methods, it only remains to constrain s. If we take $s = 3(1-\phi_m)/R$ as the specific surface area of monodispersed spheres of radius R in a volume (sphere volume fraction $1 - \phi_m$) Equation 1 becomes the more familiar $k = \phi_m^3 R^2/\left(9C(1-\phi_m)^2\right)$. For magma mush, a model of this form is used commonly (e.g., Bachmann & Bergantz, 2004).

For cuboids with three independent axis lengths a, b, and c, the s is given explicitly by (adapted from Bretagne et al. (2023))

$$s = 2(1-\phi_m)\left(\frac{1}{a} + \frac{1}{b} + \frac{1}{c}\right) \tag{2}$$

and so for packs of cuboids, the Kozeny-Carman law given in Equation 1 becomes

$$k = \frac{\phi_m^3}{4C(1-\phi_m)^2}\left(\frac{1}{a}+\frac{1}{b}+\frac{1}{c}\right)^{-2} \quad (3)$$

This implies that if the cuboid lengths a, b, and c and the melt fraction ϕ_m can be determined, so too can the permeability. Bretagne et al. (2023) validated the efficacy of Equation 3 for 3D simulated volumes of packed cuboids for which $b = c$ (i.e., square-ended cuboids), However, some key aspects of this hypothesis still require testing, specifically does Equation 3 remain valid for: (a) cuboids for which $b \neq c$; (b) particles that are not cuboids but which could be approximated as cuboids; and (c) given the sensitivity of k to s (via s^2 in Equation 1), is Equation 3 valid for rough particles or particles for which the surface area is far larger than the particle shape might imply? Here, we provide the results of these tests of these questions.

Equation 3 is in dimensional form, which means that it is scale-dependent and k depends on not only the relative ratios of a, b, and c, but also on the magnitude of a, b, and c. In order to compare simulation results or empirical data across scales, while still testing Equation 3, we can introduce a scaling parameter, which is a reference permeability. We choose $k_s = 2(1-\phi_m)/s^2$ (Bretagne et al., 2023), which is a so-called "Stokes permeability" (Bretagne et al., 2023; Martys et al., 1994; Vasseur et al., 2021, 2022; Wadsworth et al., 2016). For some idealized systems of solid spheres in a volume, the Stokes permeability is the limiting value of k as $\phi_m \to 1$ and is related to Stokes law for the drag around a sphere. If we divide Equation 1 by this value, we retrieve a dimensionless permeability $\overline{k}$ that should be universal and scale independent and applicable across a wide range of mush types in nature and the laboratory (Vasseur et al., 2021, 2022)

$$\overline{k} = \frac{k}{k_s} = \frac{{\phi_m}^3}{2C(1-\phi_m)}. \quad (4)$$

3. Materials and Methods

3.1. Methods to Test the Permeability Model

In the crust, preserved examples of mush show that the crystals are typically intergrown or overgrown such that the crystallinity is high (Cashman et al., 2017; Sparks et al., 2019, 2022). By contrast, erupted magmas, and even what are thought of as "high crystallinity" dome lavas, are typically melt-dominated (see crystallinity ranges in Popa et al. (2021)). Therefore, during crystallization, crystal-settling (Dufek & Bachmann, 2010), or compaction (e.g., Bachmann & Bergantz, 2008) magmas on their way to becoming mush will transition through the "loose mush" window of melt fraction. That is, crystals will begin to touch one another and interact in a framework with melt between them (see Figure 1A in Holness et al. (2019)). In such loose packings, the majority of the crystals share contacts with neighboring crystals and form an interconnected structure, and the degree of intergrowth is low. It is these loose mush materials that we emulate here. To create real loose mush analogs in the laboratory with a range of particle geometries, we represent the crystals by confectionary: either near cubic or cuboidal shape, smooth faced fudge chunks, or non-cuboid rough sugar crystals (Figure 1).

We load particles randomly into a 20 mm diameter cylindrical centrifuge tube, ensuring at least 10 particles can fit across the cylinder diameter. The cylinders are shaken slightly to settle the particles into a near-random close pack, and then imaged using a Nikon XTH LC 225 kV 225°W Ultrafocus laboratory X-ray tomography scanner at the University of Strathclyde. Scans were performed at 90 kV (either 91 µA and 2 s exposure, or 209 µA and 1 s exposure depending on scan) and were reconstructed using built-in algorithms to give a 2,000 voxel image with 16 µm voxel resolution. The scans of loosely packed particles produce density contrast grayscale data (Figures 1a and 1c). Visualization and segmentation of the solid and interstitial phases into binary images were performed using Avizo© (Figures 1b and 1d, see Dobson et al. (2020) for more details on the methodology in Avizo©). The confectionary is segmented as a whole entity and is analogous to natural loosely packed crystals in a mush; the interstitial phase exists as one continuous connected material in the 3D data and represents the interstitial melt in our analogue magma mush system.

In order to determine a permeability, we select the lattice Boltzmann method (LBM) for fluid flow simulation. Although early versions of the LBM (McNamara & Zanetti, 1988) suffered from the same high computational expense as alternative methods, such as smoothed particle hydrodynamics (Jiang & Sousa, 2008) or lattice gas autonoma (Frisch et al., 1986), advances in LBM efficiency have made it a go-to mesoscopic fluid flow tool (Qian et al., 1992). In addition to computational efficiency, the LBM allows a user to implement solid boundaries

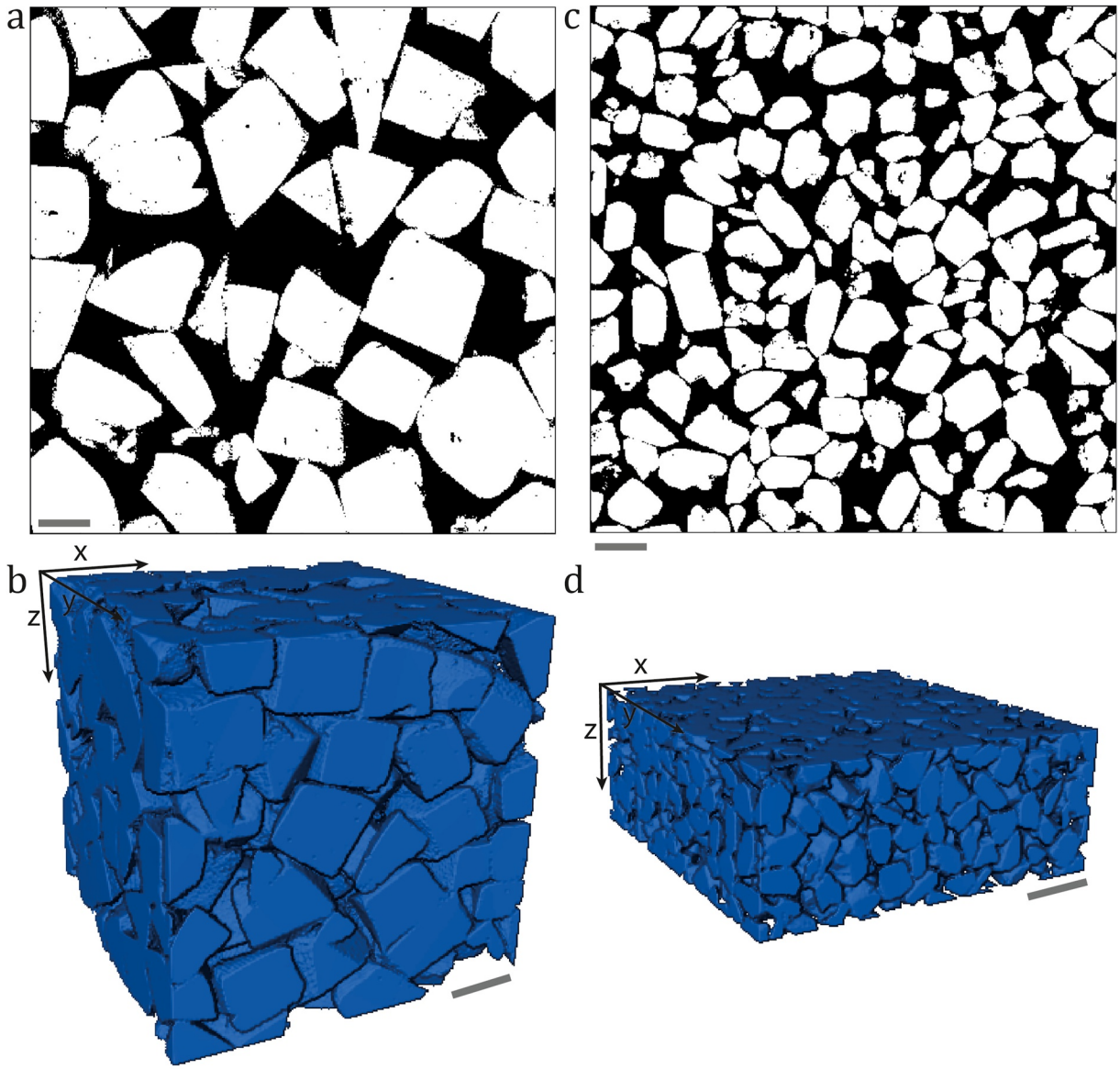

Figure 1. Renderings of representative volume of panels (a)–(b) the packed fudge chunks, and panels (c)–(d) the packed sugar crystals. In panels (a), (c), a 2D slice representation of the domains and in panels (b), (d), the 3D renders of the binary data where the blue phase represents the confectionary and the "melt" phase is represented by void. In the 2D representations, the scale bar represents 100 μm and in 3D, the scale bar is 200 μm.

of arbitrary complexity without computational penalty (i.e., without the need for local mesh density increases around complex boundaries). The LBM has been shown to outperform conventional finite volume fluid dynamic methods for complex pore geometries (Bernsdorf et al., 1999; Breuer et al., 2000; Krüger et al., 2017). For these reasons, LBM is the method we use.

The binary data sets were loaded into the lattice-Boltzmann fluid flow simulation tool LBflow (Llewellin, 2010a, 2010b) which is designed for determining fluid flow through complex porous media. The input phase of interest (the porosity between the solid particles used here as a proxy for the melt fraction) is discretized into a cubic D_3Q_{15} lattice of fluid nodes. In the lattice Boltzmann simulation, we impose a uniform pressure gradient ∇p of 0.01 Pa.m^{-1} on the fluid in the numerical domain, and fluid mass is propagated through the lattice. At each simulation time step, fluid mass can move to neighboring nodes or stay at the current node. As well as this propagation, the simulation accounts for fluid collisions. This propagation and collision approach is given by the lattice Boltzmann equation (see Llewellin, 2010a, 2010b). Interactions with solid pore walls is solved for using bounceback methods (see Succi, 2001) implemented by Llewellin (2010a).

The simulation takes properties (including ∇p) in various simulation units. However, the scalings involved in the LBM allow these to be related to real fluid properties. Therefore, we can input fluid properties of our choice. We use fluid properties of viscosity $\mu = 1.8205$ Pa.s and $\rho = 1.2047$ kg.m^{-3} corresponding to the National Institute of Standards and Technology values for air at normal temperature and pressure conditions (20°C and 1 atm respectively), and therefore similar to an air permeability test in the laboratory. The simulation converges to steady flow when the average fluid speed does not change by more than 10^{-5} simulation units over 50 time-steps twice consecutively. At steady state, the principal output of the simulation is the distribution of fluid velocity vectors. We take the average fluid speed in the direction in which the pressure gradient was applied u. This speed u is then averaged for the volume, such that $\langle u \rangle = \phi_m u$. Which is then input to Darcy's law to retrieve permeability values. The initial conditions of the simulation are all chosen to ensure that the model remains in the low Reynolds number Re and low Mach number Ma regime (see Vasseur et al., 2021 for details). For our system we find $10^{-12} \leq \mathrm{Re} \leq 10^{-5}$ and $10^{-16} \leq \mathrm{Ma} \leq 10^{-9}$.

LBflow has been validated or applied using sphere packs in cubic lattice arrangements (Llewellin, 2010b; Wadsworth et al., 2017), random overlapping sphere packs (Vasseur & Wadsworth, 2017; Vasseur et al., 2020), hard sphere packs (Vasseur et al., 2021, 2022), hexagonal arrays (Vasseur & Wadsworth, 2019), fibrous porous media (Nabovati et al., 2009), sintering systems (Wadsworth et al., 2017, 2021), and basalt pore spaces (Macente et al., 2022) among others. We calculate the specific surface area s of the particle packs using a marching cubes algorithm (Lorensen & Cline, 1987) from Python's scikit-image toolbox (following Lewiner et al., 2003). This workflow yields the permeability k, the specific surface area s, and the melt fraction ϕ_m, allowing explicit validation of Equation 4.

The aim of this study includes testing the robustness of the specific surface area model in Equation 2 applied to natural shapes to show that the permeability model (Equations 3 and 4) can be used without explicitly measuring s. Here, we measure the specific surface area directly from the 3D volume of the numerical domains, but this is not always accessible to all users of permeability models. We aim to test Equation 2 so that any users can approximate the shape of anisotropic crystals/particles in loosely packed systems if they do not have access to the X-ray CT scanning methods used here. To achieve this part, we added a processing step in Avizo© wherein we apply a separation algorithm to the binary solid-liquid volumetric data. This step separates each particle into individual entities form which we can obtain the principal orthogonal axes length a, b, and c as well as 3D shape parameters. The three independent length scales can then be used to approximate particle shape without a priori knowledge of the specific surface area s.

3.2. Methods to Additionally Test the Effect of Surface Roughness

Although the scans we collected are sufficient to accurately resolve particle edges and surfaces, we can also numerically roughen the surface of the particles of the binary volumetric data by a factor f, applying a rescale algorithm to the data sets without an anti-aliasing filter. This step effectively combines locally adjacent voxels to produce lesser quality data where the surface is less smooth and thereby generating new particle shapes (Figure 2). The down sampling process is performed using scikit-image toolbox, from $f = 1$ to $f = 0.10$ where the value $f = 1$ represents no down sampling applied and the value $f = 0.10$ represents the volumetric domain that has been down sampled by a factor 10. We apply the same workflow in LBflow to each roughened data set to determine the permeability k and the specific surface area s. Our data show the efficacy of the scaling process applied to particles with non-smooth edges, but we acknowledge that this cannot readily be used without prior knowledge of s because the particles at low-f are non-cuboidal (Figure 2d). While Equation 2 is not strictly valid when the particles are non-cuboidal, the relationship $k \propto s^{-2}$ given by Equation 1 can still be tested.

3.3. Analysis Philosophy and Extrapolation

Across all of our samples/scans, we cover the porosity range $0.35 \lesssim \phi_m \lesssim 0.39$. While this is a relatively small range of porosity (or melt fraction), we supplement the primary data sets presented here with data from Bretagne et al. (2023) which covers a wider range of porosity, albeit for idealized cuboid particles. We also consider data for randomly packed hard spheres from Vasseur et al. (2021). Taken together, these data sets cover a wide range of porosity so as to represent a thorough test of our model (see Section 2). While this model has been tested to some extent by Bretagne et al. (2023), we emphasize that the model has only been tested on idealized particle

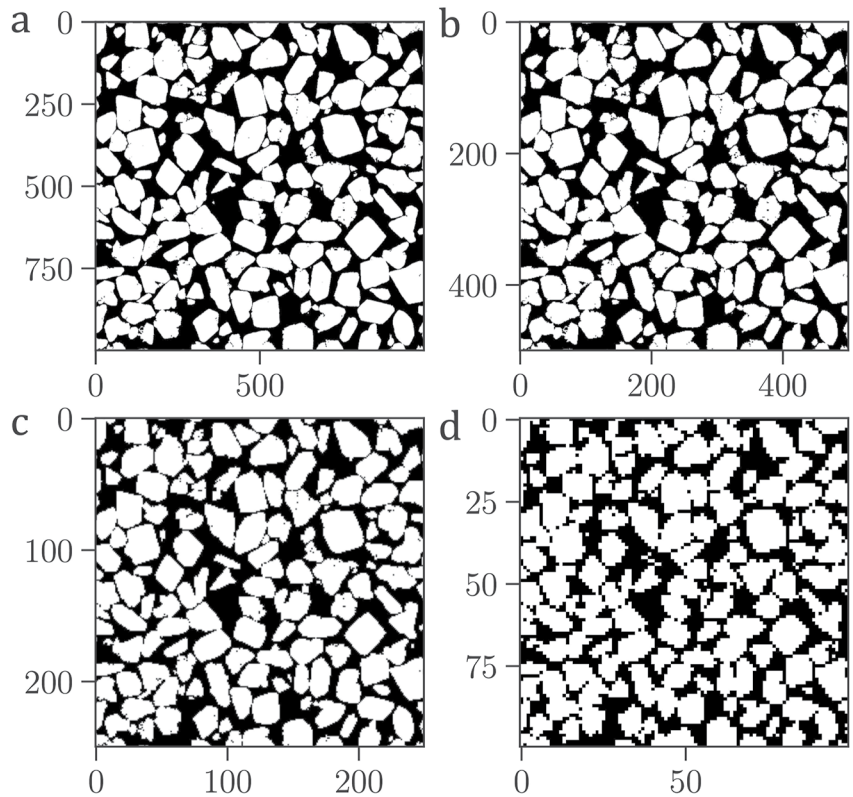

Figure 2. An example output from the roughening algorithm for (a) $f = 1$ (i.e., the domain as measured), (b) $f = 0.50$, (c) $f = 0.25$, and (d) $f = 0.10$ applied to the sugar crystals data set. The values on the x- and *y*-axes are the voxel counts.

systems and the effects of imperfect cuboid shapes, rough particles, and heterogeneities inherent in natural data have not been accounted for or tested. Here, our samples and analysis protocols aim to test the limits of the model in the case of these imperfections or points where the relatively simple geometrical assumptions of the model are invalidated.

The primary philosophy of the down-sampling method increasing surface roughness (Section 3b) is not to replicate any particular natural case (although we do envisage that mush-hosted crystals are not perfect smooth cuboids). But instead, that protocol is designed to test/demonstrate that Equation 1 is highly effective when s is known a priori.

4. Results and Analysis

The geometry of the fudge bits is cubic or cuboidal with relatively smooth-edges compared with the sugar particles which are anisometric and rough-edged (Figure 1); and represent a variable and harsh test of the simple models presented in Section 2. We test both the universal dimensionless permeability model (Equation 4) as well as the dimensional model with different methods of predicting s. In all cases, raw data for k, s, and ϕ are given in Table 1. k is determined in all three principal directions, however we discuss the results of the average of those values and use the standard deviation on that average to compute uncertainties via a standard error (e.g., in Figure 3). While the melt fraction range is only 0.35–0.39, the models we test are theoretical or semi-empirical and not subject to fitting parameters, hence if the models are validated for this melt fraction range, we can consider this a validation for a wider range of ϕ_m than explicitly tested here.

4.1. Results Using the Measured Specific Surface Area

The output values of the permeability k can be used with the measured s and ϕ_m to define the dimensionless permeability $\overline{k} = ks^2/(2C(1-\phi_m))$, equivalent to Equation 4. By normalizing the permeability data k by the Stokes permeability k_s, thereby making the data dimensionless, we isolate the effect of the melt fraction ϕ_m on the permeability. In Table 1, the permeability data shows variations of up to 2.5 orders of magnitude for a relatively small melt fraction range (0.05), however once normalized to $\overline{k}$, the data collapse to a cluster relatively close

Table 1
Raw Data for Permeability in the 3 Directions, the Specific Surface Area, Shrinking Factor, and Melt Fraction

Name	Shrinking factor	Melt fraction	Specific surface area (m^{-1})	Perm x (m^2)	Perm y (m^2)	Perm z (m^2)
Fudge bits	1.000	0.365	34390.27	1.18×10^{-11}	1.11×10^{-11}	1.54×10^{-11}
	0.500	0.354	55853.46	3.02×10^{-12}	3.93×10^{-12}	3.68×10^{-12}
	0.333	0.350	82000.75	1.42×10^{-12}	1.74×10^{-12}	1.68×10^{-12}
	0.250	0.354	99901.65	9.39×10^{-13}	1.09×10^{-12}	1.14×10^{-12}
	0.200	0.350	125451.00	$6.02 \times 10-^{13}$	6.80×10^{-13}	7.14×10^{-13}
	0.100	0.354	212487.90	1.99×10^{-13}	2.13×10^{-13}	2.41×10^{-13}
	0.067	0.349	297233.20	9.73×10^{-14}	1.02×10^{-13}	1.17×10^{-13}
	0.050	0.353	370835.00	6.54×10^{-14}	6.81×10^{-14}	7.90×10^{-14}
Sugar crystals	1.000	0.375	59397.05	3.34×10^{-12}	3.38×10^{-12}	3.70×10^{-12}
	0.500	0.390	105453.30	1.17×10^{-12}	1.23×10^{-12}	1.22×10^{-12}
	0.333	0.383	154884.90	5.06×10^{-13}	5.37×10^{-13}	5.46×10^{-13}
	0.250	0.390	196884.20	3.19×10^{-13}	3.38×10^{-13}	3.46×10^{-13}
	0.200	0.384	242223.30	2.01×10^{-13}	2.13×10^{-13}	2.20×10^{-13}
	0.100	0.391	427365.30	6.99×10^{-14}	7.45×10^{-14}	7.71×10^{-14}
	0.067	0.383	588604.00	3.80×10^{-14}	3.99×10^{-14}	4.21×10^{-14}
	0.050	0.390	721765.10	2.77×10^{-14}	2.94×10^{-14}	3.07×10^{-14}

to the model with $C = 5$ (Röding et al., 2020; Figure 3a), regardless of whether the data have been roughened ($f < 1$) or not ($f = 1$). This demonstrates that the roughening does not affect the universality of Equation 4 when s is known. If we let C be an adjustable parameter, we can use a least-squares regression technique to minimize for the best-fit value of C. Given the relatively small differences in ϕ_m across all data, this is done by minimizing for the logarithm of the $\bar{k}$ data. We perform this minimization using all data (including the numerical cuboid data from Bretagne et al. (2023) or with each data set individually (Table 2, Figure 3b) and show the result with the best-fit C for the combination of the fudge and sugar crystals (i.e., $C = 4.01 \pm 0.24$). Zoomed in, the data fall closer to the model using $C = 4.01$ (Figure 3b). However, regardless the value of C, the slope of the data in

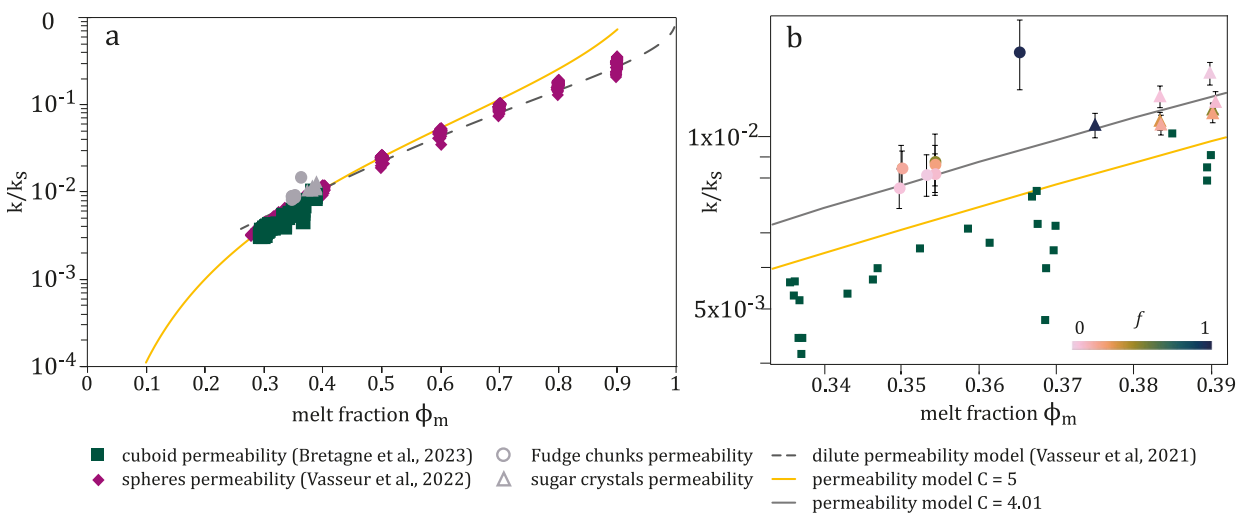

Figure 3. The normalized permeability $\bar{k}$ as a function of the inter-particle phase volume fraction ϕ_m with measured s. (a) The data from this study with roughened particles $f < 1$ values and non-roughened particles at $f = 1$. (b) A zoom-in on the data from panel (a) and including the best-fit Equation 4. Also shown are the data from Bretagne et al. (2023) for cuboid simulations, and the model (Equation 4) with $C = 5$ and for a best fit value of $C = 4.01$. For comparison, we also show hard sphere simulations from Vasseur et al. (2021, 2022), as well as the dilute permeability model which determines the prediction of Equation 4 from moderate ϕ_m.

Table 2
The Results of Fitting for the Coefficient C in Equation 4

Sample family	Best fit C	95% confidence interval	99% confidence interval
Cake topping data ($n = 16$)	4.01	±0.24	±0.33
Fudge chunks only ($n = 8$)	3.79	±0.37	±0.53
Sugar crystals only ($n = 8$)	4.24	±0.25	±0.37
Square-ended cuboids (Bretagne et al., 2023; $n = 92$)	5.83	±0.10	±0.14
All above data ($n = 108$)	5.52	±0.17	±0.22

Figure 3 matches well the Equation 4 prediction. We note that the variability of best-fit C is small and typically within minimization error of our expected $C = 5$ value. Therefore, for this small range of ϕ_m, we consider C to be a constant regardless of particle shape.

For comparison, Figure 3a also shows the data for hard sphere simulations and an associated model specifically for the permeability of hard spheres in a dilute system (Vasseur et al., 2021, 2022). This is shown here for completeness, and to demonstrate that solutions for spherical particles can, if scaled correctly, provide similar universal results as those for anisometric particles such as cuboids, fudge, and sugar.

4.2. Using the Cuboid Approximation to Find the Specific Surface Area

While Equation 4 appears effective across all data sets when s is a measured quantity, we acknowledge that in most practical scenarios of interest, s is not readily measured. However, instead, the axes lengths and shape of crystals can be measured in 2D, or in 3D, more easily. Therefore, next we aim to test our model when we take crystal axis lengths to predict an idealized s value, rather than taking the measured s.

The measured a-, b-, c-axes for each particle are used to define the specific surface area of each via Equation 2, and because there is a distribution of axis lengths in each sample, we then take an average of each of these which we term $\langle a \rangle$, $\langle b \rangle$, and $\langle c \rangle$, respectively. The standard deviation σ on each of those averages is set as the error on the axis length distributions (σ_a, σ_b, and σ_c). For the fudge chunks, $N = 79$ and for the sugar crystals, $N = 361$. These are used to determine s and an uncertainty on s (using Equation 2), assuming that this represents an approximate s from the average crystal shape in the pack. The output of these steps is a value for k_s derived from the crystal shape determinations, and which can be used to compute $\overline{k}$ for each sample. We test this with the un-roughened data at $f = 1$ because the approach here relies on the data being close to cuboidal and smooth.

In Figure 4 we show the result of the steps outlined above for the pack of fudge chunks and the pack of sugar crystals. Figure 4a shows the normalized count distribution of the crystal size for each sample. In Figure 4b, we show the result of the computation of the permeability k. We do this in dimensional space (i.e., k and not $\overline{k}$; using Equation 3 and not Equation 4). The difference between the data computed using the cuboid approximation, and the same data for which s is measured directly is a difference of less than 0.5 log units of k in the case of both the sugar crystals and fudge chunks. We conclude therefore that any prediction made using the model presented here (Equation 3) with a cuboid approximation for the specific surface area, can be accurate to within 0.5 log units when $C = 4.01$.

5. Discussion

Here we explore and extend our results in a few key ways. First, we provide the limits of applicability of our models. Second, we propose a method to find the permeability from a 2D thin section of a cumulate rock for users that do not have access to 3D scans. And third, we explore the implications of our findings for real mush systems.

5.1. The Limits of Applicability at High and Low Melt Volume Fraction ϕ_m

Like all scaling approaches, the model tested here has limits beyond which it should not be applied. The limits as $\phi_m \to 1$ are best understood by comparing the prediction of Equation 4 with those given by the dilute expansions of k_s (i.e., the "Stokes permeability"). These two competing predictions converge at the range of ϕ_m that packed particles used here occupy (see Figure 4). However, as particle packing densities ϕ drop (i.e., as ϕ_m

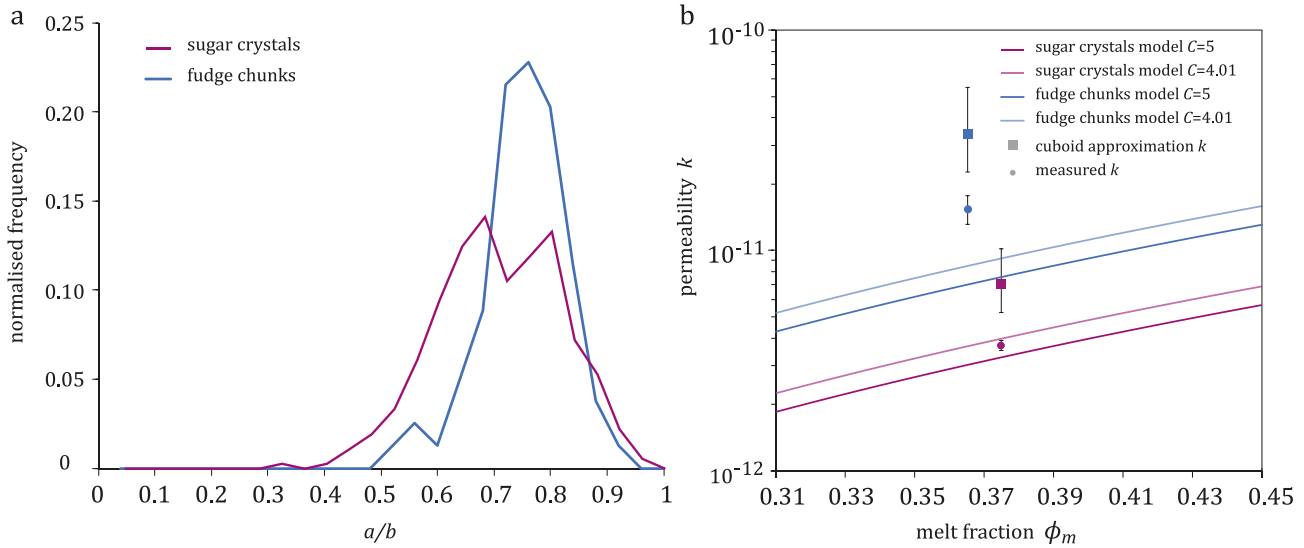

Figure 4. (a) The distribution of crystal lengths in the fudge chunks sample, and the sugar crystal sample. (b) The permeability of the fudge chunks and the sugar crystals using two methods: (1) using the measured s (as given in Figure 3); and (2) using s predicted by the cuboid approximation using the mean values given in panel (a) and the associated errors.

increases) the dilute expansion model fits better. The point at which our universal model and the dilute model diverge substantially ($\phi_m \geq 0.6$) provides a good upper limit of applicability of Equation 4, and is consistent with arguments given in Vasseur and Wadsworth (2017). Using Equation 4 at $\phi_m \geq 0.6$ will overestimate the permeability of mush. The limits as $\phi_m \to 0$ below which Equation 4 should not be used is formally given by the maximum random close packing of particles, which occurs at a particle volume fraction ϕ'. Bretagne et al. (2023) propose a functional form for this value as a function of the aspect ratio of square-ended cuboids. However, here, with triaxial cuboids, this function is not strictly valid and ϕ' is not well known. At $\phi > \phi'$ magma mush is no longer "loose" and some intergrowth, overgrowth, or deformation of the crystals must have occurred (Bretagne et al., 2023; Holness, 2018). The lowest ϕ_m determined by Bretagne et al. (2023) was approximately $\phi_m = 0.35$ and therefore we consider this value the lower limit of applicability of the model presented here (Equation 4). Based on these arguments, the model applicability window is $0.35 \leq \phi_m \leq 0.60$. Below these limits, a percolation model is required (e.g., Martys et al., 1994; Vasseur et al., 2021, 2022; Vasseur & Wadsworth, 2017; Wadsworth et al., 2016), and above these limits a dilute expansion model is required (Sangani & Acrivos, 1982; Vasseur et al., 2021, 2022).

5.2. Finding a Permeability From a 2D Thin Section

Using standard petrological methods, it is rare to have the kind of 3D data presented here, especially for silicic magmas. The most widely used X-ray computed tomography (XCT) methods can be highly effective when there is an attenuation contrast between the "crystal" and "melt" phases. In our analogue samples, the interstitial volume was air, and so the high attenuation contrast makes segmentation of phases easy, and ϕ_m allows easy separation of the individual particles. In natural cumulate samples—an erupted and quenched piece of magma mush—the interstitial melt can solidify or crystallize into the same phases as the mush (e.g., Humphreys, 2009; Morse, 1998; Wager et al., 1960), or into phases with only a small attenuation contrast, making the segmentation and separation processes challenging. More advanced phase contrast XCT and diffraction contrast tomography that can support effective image analysis for samples with low contrast are becoming more accessible. 2D analytic techniques such as thin section microscopy, on the other hand, are far more common. Hence, in this section we develop a methodology for users who only have access to 2D quantitative data to obtain accurate permeability predictions.

The size and shape values of crystals can be acquired from the 2D data (here a numerically generated thin section). Then 2D-to-3D conversion algorithms can be used to reconstruct 3D shapes (Mangler et al., 2022; Morgan & Jerram, 2006). Once one obtains the three orthogonal axes of the particle shapes, the permeability model (Equation 3) can be applied to predict the permeability of a natural mush. To test this workflow, first, we

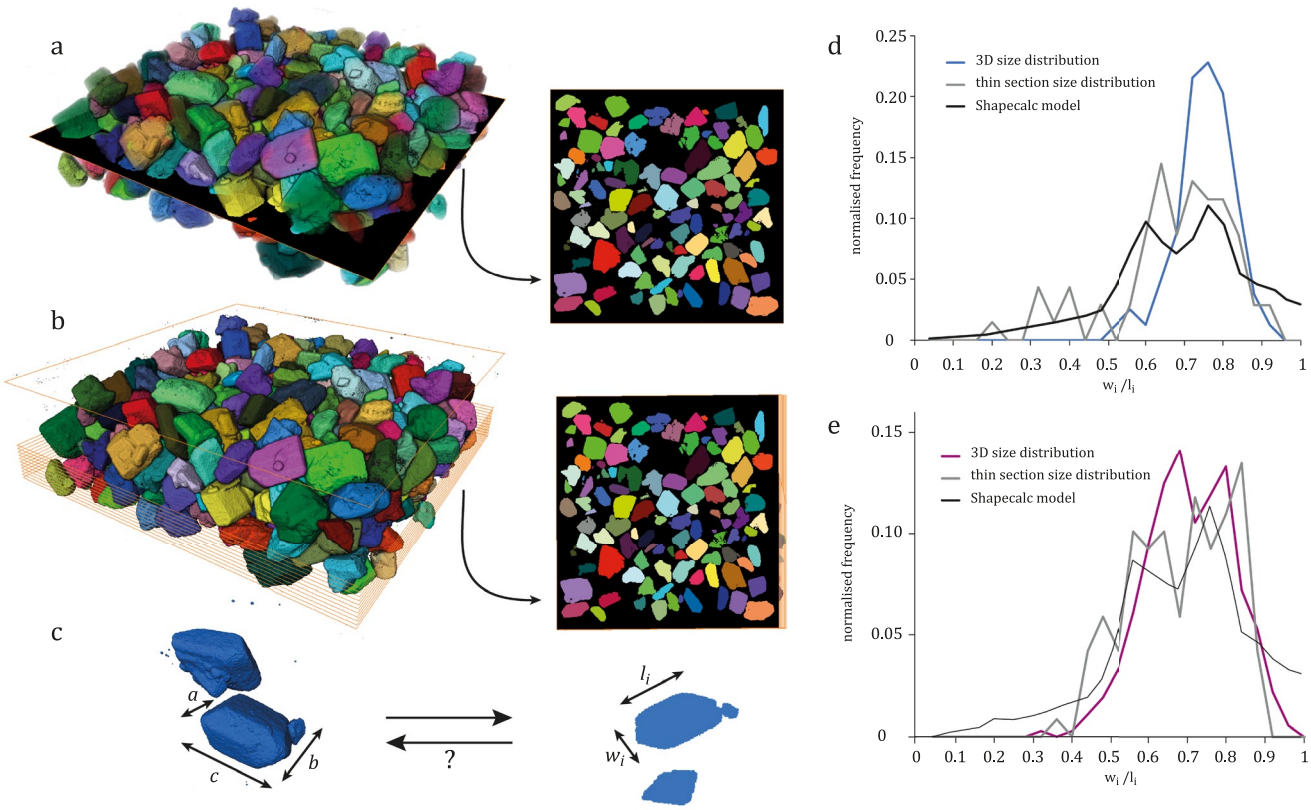

Figure 5. The process of taking a layer of 3D particles and generating a 2D slice and associated 2D w and l data. (a) An example of a 2D slice from the stack of slices. (b) A 3D render of fudge chunks with a sequence of 2D "virtual sections" cut through it. (c) Defining the cuboid axis in 3D and in 2D. Panels (d) and (e) show the associated distributions of the ratio w_i/l_i that are found from analyzing the shapes in panels (a) and (b), respectively. Also shown in panels (d) and (e) are the best-fit ShapeCalc (Mangler et al., 2022) distributions of cuboid cuts, which relates to a best-fit single cuboid shape.

define a 2D "slice" through the 3D volumes to generate a virtual thin section. This method effectively cuts the crystals in a plane and, depending on the orientation of the crystals, will result in a distribution of intersection length-scales (Figure 5). We then extract the orthogonal maximum and minimum axis lengths (the maximum and minimum Feret diameters) of each particle that we can observe in the 2D plane, which we term w_i and l_i, respectively (Figures 5a and 5c). As these 2D slices are virtual, we can produce multiple thin sections in many orientations and locations within the larger sample, effectively generating many pseudo-thin section data sets (Figure 5b). The distributions of the measured w_i/l_i ratios (Figures 5d and 5e) cannot be used directly with Equation 2, because their relationship to a, b, and c (the three "true" axes) of the 3D objects needs to be established.

To estimate the true axis lengths and allow direct application of our model, we use ShapeCalc (Mangler et al., 2022), which enables the projection of the distribution of $w_i$andl_i measured on a 2D data set into their estimated 3D crystal shape. This model yields normalized axis lengths s, the small axis, i, the intermediate axis, and l, the long axis. These represent the true axis lengths a, b, and c normalized to a, such that $s = a/a = 1$, $i = b/a$ and $l = c/a$. Higgins (1994) demonstrated that for a population of randomly oriented anisotropic 3D objects of same size and shape, the intersection long axis l_i is close to the true intermediate axis b and the intersection short axis w_i is close to the true short axis a. Therefore, $l_i \approx b$ or $w_i \approx a$. If we assume $a = w_i$, then we have $b = iw_i$ and $c = lw_i$.

Applying this workflow, we can then apply Equations 2 and 4 to the 2D virtual section data. We find that this approach works very well (Figure 6), and the propagated uncertainty on the output permeabilities is within error of both the model (Equation 3) and the measured result from LBflow with the marching cubes algorithm to find s. This demonstrates that our model, coupled with ShapeCalc, can be used to convert 2D thin section observations of packed crystal geometries, into a bulk material permeability for individual cumulate samples.

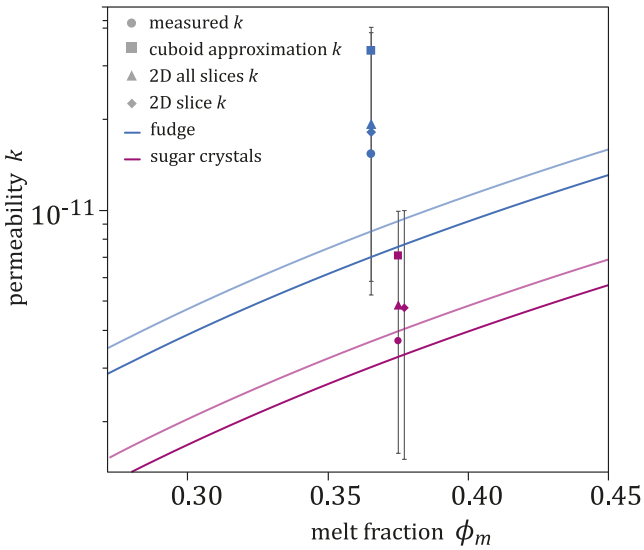

Figure 6. The results of the 2D-to-3D approach outlined here, compared with the direct result from LBflow shown in Figure 4 and the model given by Equation 3. The difference between the data from LBFlow and the projected 2D slice data (lozenges) is only of 0.07 orders of magnitude and 0.11 orders of magnitude for the fudge bits and the sugar crystals, respectively. The difference between the data from LBFlow and the projected 2D all slice data (triangles) is only of 0.10 orders of magnitude and 0.12 orders of magnitude for the fudge bits and the sugar crystals, respectively. The uncertainty on k in the 2D-to-3D method arises from propagating the uncertainty on a, b, and c from the standard deviation of w_i and l_i, which can be substantial.

5.3. Natural Magma Mush

Equations 1, 3, and 4 are all isotropic models that do not predict a full permeability tensor, nor a permeability that depends on shear strain in any manner. This is consistent with the widely used models that are embedded in magma mush melt migration solutions (Bachmann & Bergantz, 2004; Jackson et al., 2018) and indeed in general formulations for melt migration in analogous partially molten systems (e.g., McKenzie, 1984) or compaction of crystal-rich plugs even in flowing systems (e.g., Lecampion & Garagash, 2014). However, the melt percolation and extraction timescales from mush predicted from these extraction models are often many orders of magnitude in timescale slower than recorded by chronometers that track extraction processes (e.g., Holness, 2018). This has led to models that invoke shear strain and a resultant anisotropy development driving high permeability in one direction, perhaps at the expense of efficient permeable channels in the perpendicular direction (Liu & Lee, 2020), and large-scale simulations of mush dynamics that show kinematics involve the definition and evolution of a fabric tensor (Bergantz et al., 2017). This fabric tensor could be used to compute a local but volume-averaged permeability tensor description (Bergantz et al., 2017). In any anisotropic model, the scaling for permeability via a scalar specific surface area (e.g., Equation 1) will not hold, or will require additional scaling via a fabric deformation correction.

While our model is not applicable to anisotropic systems, our approach grounds solutions in the specific microstructures of mushes, accounting for the complex crystal morphologies involved, and so provides a clear direction for developing the anisotropic models, from readily producible textures produced easily in a laboratory setting and amenable to XCT techniques. Our model formulation is specific to what we term "loose mush" (see Section 1). That is, mush for which crystal-crystal intergrowth or overgrowth is minimal, and for which the mush is isotropic and simply analogous to crystals at their maximum random close packing fraction. Therefore, a tenable future step would be to extend these models to overlapping cuboid systems where ϕ_m can drop to values below the limits explored here (see Section 5a). Indeed, for overlapping objects in a volume, ϕ_m can drop to a critical value below which the system as a whole becomes impermeable—termed the percolation threshold ϕ_c (Colombier et al., 2020; Vasseur & Wadsworth, 2017; Wadsworth et al., 2021). This parameter has not been determined for systems of magma mush, but constraint of this critical percolation property, as well as s down to low-ϕ_m would allow permeability models to be extended down from the "loose mush" regime into the "intergrown mush" regime.

5.4. Applying This Model

We suggest that our model can be applied to scenarios where the melt fraction is relatively high such that crystals are at their maximum packing, but not [yet] intergrown or overgrown. In that high melt fraction range, there are two basic modes of application of our model. First, if the specific surface area of a sample can be determined a priori, then Equation 1 can be applied directly using $C = 5$. This mode of application is anticipated to be possible where a user has access to 3D XCT of a mush, and can use algorithms similar to those used here to both isolate the crystal framework and to determine the specific surface of that crystal framework. However, where this is not possible, the second basic mode of application is to make a cuboidal assumption about the crystal shapes and to constrain the size of the mutually perpendicular axes. We demonstrate that an average of a population of crystal axis sizes performs well. Then, using Equation 3, the user can estimate the permeability. Based on this work, the uncertainty associated with the first mode of application may be 0.1 log units, whereas the uncertainty on the second mode of application may be up to 0.5 log units. Finally, if the crystals are especially rough or deviate from cuboidal, then an independent measure of the specific surface area will be required. However, once known, we show that Equation 1 is effective in this range of melt fraction regardless of the specific surface, the roughness, or the particle shapes.

6. Conclusions

In this contribution, we have expanded the relatively simple biaxial cuboid model presented in Bretagne et al. (2023) to account for the triaxial nature of natural crystal shape. We have validated that expanded form of the model using real XCT data for mush analogs, and identified the need for a minor adjustment of the constant C (albeit with reasonable efficacy for the forward model with $C = 5$). We have also shown that the model is accurate to within 0.2–0.5 log units when the axes of particles approximated from 2D thin section derived measurements; opening up the possibility that mush permeability can be extracted as part of a general petrological workflow in any laboratory.

As with Bretagne et al. (2023), we emphasize that the permeability model presented here can be orders of magnitude different from existing approaches. While our model (Equation 3) is similar in form (and based on the same starting point) as the Kozeny-Carman model given in Bachmann and Bergantz (2004), the shape-dependence of permeability that we apply renders the predictions of our model dramatically different from those of $k = \phi_m{}^3 a^2 / \left(150(1-\phi_m)^2\right)$ with a fixed single crystal "size" a. Therefore, we propose that not only does our model include the effect of crystal shape, which should be incorporated in mush permeability models, but it also gives higher permeability predictions than existing approaches. If embedded in any existing melt migration model, the higher permeabilities predicted here would result in greater fluxes and shorter overall transport timescales for a given set of conditions. Therefore, there are direct implications of our result for crustal melt movement models.

Data Availability Statement

All raw and processed permeability data and processed X-ray 3D data pertaining to this manuscript are provided in Bretagne et al. (2023) and available for download from https://doi.org/10.5281/zenodo.8349055. The software Avizo© is available by industrial paid license.

Acknowledgments
We thank Madeleine Humphreys, Martin Mangler, Alex Iveson, Amanda Lindoo, Charline Lormand, Katie Schofield, and Gemma Brown, for fascinating discussions about magma mush dynamics during "mush meetings" at Durham University, led by Madeleine Humphreys. We thank Donald Dingwell for facilitating the contribution of J. Vasseur and for general discussion. We acknowledge funding from a Durham Doctoral Scholarship provided to E. Bretagne, and the Natural Environment Research Council Standard Grant "Magma mush eruptibility: The lifetime of mobile magma" NE/T000430/1. We acknowledge access to the OGIC XCT facility at Strathclyde which was supported by EP/T023198/1, and NE/T00908X/2. We also thank two anonymous reviewers for their constructive feedback and substantial improvements brought to the manuscript.

References

Annen, C. (2009). From plutons to magma chambers: Thermal constraints on the accumulation of eruptible silicic magma in the upper crust. *Earth and Planetary Science Letters*, *284*(3–4), 409–416. https://doi.org/10.1016/j.epsl.2009.05.006

Bachmann, O., & Bergantz, G. W. (2004). On the origin of crystal-poor rhyolites: Extracted from batholithic crystal mushes. *Journal of Petrology*, *45*(8), 1565–1582. https://doi.org/10.1093/petrology/egh019

Bachmann, O., & Bergantz, G. W. (2008). Rhyolites and their source mushes across tectonic settings. *Journal of Petrology*, *49*(12), 2277–2285. https://doi.org/10.1093/petrology/egn068

Bergantz, G. W., Schleicher, J. M., & Burgisser, A. (2017). On the kinematics and dynamics of crystal-rich systems. *Journal of Geophysical Research: Solid Earth*, *122*(8), 6131–6159. https://doi.org/10.1002/2017jb014218

Bernsdorf, J., Durst, F., & Schäfer, M. (1999). Comparison of cellular automata and finite volume techniques for simulation of incompressible flows in complex geometries. *International Journal for Numerical Methods in Fluids*, *29*(3), 251–264. https://doi.org/10.1002/(sici)1097-0363(19990215)29:3<251::aid-fld783>3.0.co;2-l

Bretagne, E., Wadsworth, F. B., Vasseur, J., & Dobson, K. J. (2023). A scaling for the permeability of loose magma mush validated using X-ray computed tomography of packed confectionary in 3D and estimation methods from 2D crystal shapes [Dataset]. Zenodo. https://doi.org/10.5281/zenodo.8349055

Breuer, M., Bernsdorf, J., Zeiser, T., & Durst, F. (2000). Accurate computations of the laminar flow past a square cylinder based on two different methods: Lattice-Boltzmann and finite-volume. *International Journal of Heat and Fluid Flow*, *21*(2), 186–196. https://doi.org/10.1016/s0142-727x(99)00081-8

Cashman, K. V., Sparks, R. S. J., & Blundy, J. D. (2017). Vertically extensive and unstable magmatic systems: A unified view of igneous processes. *Science*, *355*(6331), 3055. https://doi.org/10.1126/science.aag3055

Cheadle, M. J., Elliott, M. T., & McKenzie, D. (2004). Percolation threshold and permeability of crystallizing igneous rocks: The importance of textural equilibrium. *Geology*, *32*(9), 757–760. https://doi.org/10.1130/g20495.1

Colombier, M., Wadsworth, F. B., Scheu, B., Vasseur, J., Dobson, K. J., Cáceres, F., et al. (2020). In situ observation of the percolation threshold in multiphase magma analogues. *Bulletin of Volcanology*, *82*(4), 1–15. https://doi.org/10.1007/s00445-020-1370-1

Dobson, K. J., Allabar, A., Bretagne, E., Coumans, J., Cassidy, M., Cimarelli, C., et al. (2020). Quantifying microstructural evolution in moving magma. *Frontiers in Earth Science*, *8*, 287. https://doi.org/10.3389/feart.2020.00287

Dufek, J., & Bachmann, O. (2010). Quantum magmatism: Magmatic compositional gaps generated by melt-crystal dynamics. *Geology*, *38*(8), 687–690. https://doi.org/10.1130/g30831.1

Ergun, S. (1952). Determination of geometric surface area of crushed porous solids. *Analytical Chemistry*, *24*(2), 388–393. https://doi.org/10.1021/ac60062a033

Frisch, U., Hasslacher, B., & Pomeau, Y. (1986). Lattice-gas automata for the Navier–Stokes equation. *Physical Review Letters*, *56*(14), 1505–1508. https://doi.org/10.1103/physrevlett.56.1505

Hersum, T. (2009). Consequences of crystal shape and fabric on anisotropic permeability in magmatic mush. *Contributions to Mineralogy and Petrology*, *157*(3), 285–300. https://doi.org/10.1007/s00410-008-0334-9

Hersum, T., Hilpert, M., & Marsh, B. (2005). Permeability and melt flow in simulated and natural partially molten basaltic magmas. *Earth and Planetary Science Letters*, *237*(3–4), 798–814. https://doi.org/10.1016/j.epsl.2005.07.008

Higgins, M. D. (1994). Numerical modeling of crystal shapes in thin sections: Estimation of crystal habit and true size. *American Mineralogist*, *79*(1–2), 113–119.

Hildreth, W., & Wilson, C. J. (2007). Compositional zoning of the Bishop Tuff. *Journal of Petrology*, *48*(5), 951–999. https://doi.org/10.1093/petrology/egm007

Holness, M. B. (2018). Melt segregation from silicic crystal mushes: A critical appraisal of possible mechanisms and their microstructural record. *Contributions to Mineralogy and Petrology*, *173*(6), 1–17. https://doi.org/10.1007/s00410-018-1465-2

Holness, M. B., Stock, M. J., & Geist, D. (2019). Magma chambers versus mush zones: Constraining the architecture of sub-volcanic plumbing systems from microstructural analysis of crystalline enclaves. *Philosophical Transactions of the Royal Society A*, *377*(2139), 20180006. https://doi.org/10.1098/rsta.2018.0006

Humphreys, M. C. (2009). Chemical evolution of intercumulus liquid, as recorded in plagioclase overgrowth rims from the Skaergaard intrusion. *Journal of Petrology*, *50*(1), 127–145. https://doi.org/10.1093/petrology/egn076

Jackson, M. D., Blundy, J., & Sparks, R. S. J. (2018). Chemical differentiation, cold storage and remobilization of magma in the Earth's crust. *Nature*, *564*(7736), 405–409. https://doi.org/10.1038/s41586-018-0746-2

Jiang, F., & Sousa, A. C. M. (2008). Smoothed particle hydrodynamics modelling of transverse flow in randomly aligned fibrous porous media. *Transport in Porous Media*, *75*(1), 17–33. https://doi.org/10.1007/s11242-008-9206-z

Krüger, T., Kusumaatmaja, H., Kuzmin, A., Shardt, O., Silva, G., & Viggen, E. M. (2017). The lattice Boltzmann method. *Springer International Publishing*, *10*(978–3), 4–15.

Lecampion, B., & Garagash, D. I. (2014). Confined flow of suspensions modelled by a frictional rheology. *Journal of Fluid Mechanics*, *759*, 197–235. https://doi.org/10.1017/jfm.2014.557

Lewiner, T., Lopes, H., Vieira, A. W., & Tavares, G. (2003). Efficient implementation of marching cubes' cases with topological guarantees. *The Journal of Graphics Tools*, *8*(2), 1–15. https://doi.org/10.1080/10867651.2003.10487582

Liu, B., & Lee, C. T. (2020). Large silicic eruptions, episodic recharge, and the transcrustal magmatic system. *Geochemistry, Geophysics, Geosystems*, *21*(9), e2020GC009220. https://doi.org/10.1029/2020gc009220

Liu, B., & Lee, C. T. (2021). Fast melt expulsion from crystal-rich mushes via induced anisotropic permeability. *Earth and Planetary Science Letters*, *571*, 117113. https://doi.org/10.1016/j.epsl.2021.117113

Liu, L., Li, Z., Jiao, Y., & Li, S., (2017). Maximally dense random packings of cubes and cuboids via a novel inverse packing method. *Soft Matter*, *13*(4), 748–757.

Llewellin, E. W. (2010a). LBflow: An extensible lattice Boltzmann framework for the simulation of geophysical flows. Part I: Theory and implementation. *Computers and Geosciences*, *36*(2), 115–122. https://doi.org/10.1016/j.cageo.2009.08.004

Llewellin, E. W. (2010b). LBflow: An extensible lattice Boltzmann framework for the simulation of geophysical flows. Part II: Usage and validation. *Computers & Geosciences*, *36*(2), 123–132. https://doi.org/10.1016/j.cageo.2009.08.003

Lorensen, W. E., & Cline, H. E. (1987). Marching cubes: A high resolution 3D surface construction algorithm. *ACM Siggraph Computer Graphics*, *21*(4), 163–169. https://doi.org/10.1145/37402.37422

Macente, A., Dobson, K. J., MacDonald, J., Wadsworth, F. B., & Vasseur, J. (2022). The evolution of paleo-porosity in Basalts: Reversing pore-filling mechanisms using X-ray computed tomography. *Transport in Porous Media*, *145*(3), 697–717. https://doi.org/10.1007/s11242-022-01869-2

Mangler, M. F., Humphreys, M., Wadsworth, F. B., Iveson, A. A., & Higgins, M. D. (2022). Variation of plagioclase shape with size in intermediate magmas: A window into incipient plagioclase crystallisation. *Contributions to Mineralogy and Petrology*, *177*(6), 1–21. https://doi.org/10.1007/s00410-022-01922-9

Martys, N. S., Torquato, S., & Bentz, D. P. (1994). Universal scaling of fluid permeability for sphere packings. *Physical Review E*, *50*(1), 403–408. https://doi.org/10.1103/physreve.50.403

McKenzie, D. (1984). The generation and compaction of partially molten rock. *Journal of Petrology*, *25*(3), 713–765. https://doi.org/10.1093/petrology/25.3.713

McNamara, G. R., & Zanetti, G. (1988). Use of the Boltzmann equation to simulate lattice gas automata. *Physical Review Letters*, *61*(20), 2332–2335. https://doi.org/10.1103/physrevlett.61.2332

Morgan, D. J., & Jerram, D. A. (2006). On estimating crystal shape for crystal size distribution analysis. *Journal of Volcanology and Geothermal Research*, *154*(1–2), 1–7. https://doi.org/10.1016/j.jvolgeores.2005.09.016

Morse, S. A., & McBirney, A. R. (1998). Is the cumulate paradigm at risk? An extended discussion of the cumulate paradigm reconsidered. *The Journal of Geology*, *106*(3), 367–372. https://doi.org/10.1086/516029

Nabovati, A., Llewellin, E. W., & Sousa, A. C. (2009). A general model for the permeability of fibrous porous media based on fluid flow simulations using the lattice Boltzmann method. *Composites Part A: Applied Science and Manufacturing*, *40*(6–7), 860–869. https://doi.org/10.1016/j.compositesa.2009.04.009

Popa, R. G., Bachmann, O., & Huber, C. (2021). Explosive or effusive style of volcanic eruption determined by magma storage conditions. *Nature Geoscience*, *14*(10), 781–786. https://doi.org/10.1038/s41561-021-00827-9

Qian, Y. H., D'Humieres, D., & Lallemand, P. (1992). Lattice BGK models for Navier–Stokes equation. *Europhysics Letters*, *17*(6), 479–484. https://doi.org/10.1209/0295-5075/17/6/001

Röding, M., Ma, Z., & Torquato, S. (2020). Predicting permeability via statistical learning on higher-order microstructural information. *Scientific Reports*, *10*(1), 1–17. https://doi.org/10.1038/s41598-020-72085-5

Sangani, A. S., & Acrivos, A. (1982). Slow flow through a periodic array of spheres. *International Journal of Multiphase Flow*, *8*(4), 343–360. https://doi.org/10.1016/0301-9322(82)90047-7

Sparks, R. S. J., Annen, C., Blundy, J. D., Cashman, K. V., Rust, A. C., & Jackson, M. D. (2019). Formation and dynamics of magma reservoirs. *Philosophical Transactions of the Royal society A*, *377*(2139), 20180019. https://doi.org/10.1098/rsta.2018.0019

Sparks, R. S. J., Blundy, J. D., Cashman, K. V., Jackson, M., Rust, A., & Wilson, C. J. N. (2022). Large silicic magma bodies and very large magnitude explosive eruptions. *Bulletin of Volcanology*, *84*(1), 8. https://doi.org/10.1007/s00445-021-01510-y

Succi, S. (2001). *The lattice Boltzmann equation for fluid dynamics and beyond*. Oxford University Press.

Torquato, S. (2013). *Random heterogeneous materials*. Springer.

Tramontano, S., Gualda, G. A., & Ghiorso, M. S. (2017). Internal triggering of volcanic eruptions: Tracking overpressure regimes for giant magma bodies. *Earth and Planetary Science Letters*, *472*, 142–151. https://doi.org/10.1016/j.epsl.2017.05.014

Vasseur, J., & Wadsworth, F. B. (2017). Sphere models for pore geometry and fluid permeability in heterogeneous magmas. *Bulletin of Volcanology*, *79*(11), 1–15. https://doi.org/10.1007/s00445-017-1165-1

Vasseur, J., & Wadsworth, F. B. (2019). The permeability of columnar jointed lava. *Journal of Geophysical Research: Solid Earth*, *124*(11), 11305–11315. https://doi.org/10.1029/2019jb018118

Vasseur, J., Wadsworth, F. B., Bretagne, E., & Dingwell, D. B. (2022). Universal scaling for the permeability of random packs of overlapping and nonoverlapping particles. *Physical Review E*, *105*(4), L043301. https://doi.org/10.1103/physreve.105.l043301

Vasseur, J., Wadsworth, F. B., Coumans, J. P., & Dingwell, D. B. (2021). Permeability of packs of polydisperse hard spheres. *Physical Review E*, *103*(6), 062613. https://doi.org/10.1103/physreve.103.062613

Vasseur, J., Wadsworth, F. B., & Dingwell, D. B. (2020). Permeability of polydisperse magma foam. *Geology*, *48*(6), 536–540. https://doi.org/10.1130/g47094.1

Wadsworth, F. B., Vasseur, J., Casas, A. S., Delmelle, P., Hess, K. U., Ayris, P. M., & Dingwell, D. B. (2021). A model for the kinetics of high-temperature reactions between polydisperse volcanic ash and SO_2 gas. *American Mineralogist: Journal of Earth and Planetary Materials*, *106*(8), 1319–1332. https://doi.org/10.2138/am-2021-7691

Wadsworth, F. B., Vasseur, J., Llewellin, E. W., & Dingwell, D. B. (2017). Sintering of polydisperse viscous droplets. *Physical Review E*, *95*(3), 033114. https://doi.org/10.1103/physreve.95.033114

Wadsworth, F. B., Vasseur, J., Scheu, B., Kendrick, J. E., Lavallée, Y., & Dingwell, D. B. (2016). Universal scaling of fluid permeability during volcanic welding and sediment diagenesis. *Geology*, *44*(3), 219–222. https://doi.org/10.1130/g37559.1

Wager, L. R., Brown, G. M., & Wadsworth, W. J. (1960). Types of igneous cumulates. *Journal of Petrology*, *1*(1), 73–85. https://doi.org/10.1093/petrology/1.1.73

Wilson, C. J., Cooper, G. F., Chamberlain, K. J., Barker, S. J., Myers, M. L., Illsley-Kemp, F., & Farrell, J. (2021). No single model for supersized eruptions and their magma bodies. *Nature Reviews Earth and Environment*, *2*(9), 610–627. https://doi.org/10.1038/s43017-021-00191-7